The Astrophysical Journal, 899:125 (13pp), 2020 August 20 https://doi.org/10.3847/1538-4357/aba8a7
© 2020. The American Astronomical Society. All rights reserved.

Magnetospheric Multiscale Observations of the Off-equatorial Dipolarization Front Dynamics in the Terrestrial Magnetotail

Huimin Li[1], Congkuan Zhu[1], Lixin Guo[1], Qi Cheng[1], and O. Le Contel[2]
[1] School of Physics and Optoelectronic Engineering, Xidian University, Xi'an, People's Republic of China
[2] Laboratoire de Physique des Plasmas, CNRS-Ecole Polytechnique-Sorbonne Université-Univ. Paris Sud-Observatoire de Paris, Paris, France
Received 2019 October 9; revised 2020 July 20; accepted 2020 July 21; published 2020 August 20

Abstract

We report the Magnetospheric Multiscale observations of dynamics at an off-equatorial dipolarization front (DF) in the Terrestrial Magnetotail. Three different plasma waves, namely electromagnetic ion cyclotron (EMIC) waves, lower hybrid drift waves, and electrostatic solitary waves (ESWs), associated with different electron pitch angle distributions were detected at different subregions of a single DF. It is interesting to note that the EMIC wave was linearly polarized, associating with a parallel current as a result of the antiparallel drift of electrons in the energy range of about 0.3–2 keV. These suggest that the wave was most likely to be locally generated. This generation could be explained by the current-driven kink-like instability due to the electron drift. The current-driven instabilities may dissipate the energy of the field-aligned current at the DF and thus play important roles in the magnetosphere–ionosphere coupling. On the other hand, the detected ESWs are interpreted as multidimensional electromagnetic electron holes (EHs) which are manifestations of several distinguishing features in electric and magnetic field perturbation. The EHs with a strong positive central potential suggested the likelihood of nonlinear behavior.

Unified Astronomy Thesaurus concepts: Space plasmas (1544); Plasma astrophysics (1261)

1. Introduction

Dipolarization fronts (DFs), which are commonly observed in the central plasma sheet, are typically characterized by a sharp and large-amplitude increase in the magnetic field component normal to the neutral sheet (B_z) (Nakamura et al. 2002; Runov et al. 2009; Zhou et al. 2009a; Fu et al. 2012a; Liu et al. 2018b; Zhong et al. 2019). Some of the DFs were preceded by a minor B_z dip, and then followed by a decrease of plasma density and plasma pressure (Ohtani 2004; Runov et al. 2009; Schmid et al. 2011). A DF is usually interpreted as a boundary layer with thickness on the order of the ion inertial length or the ion gyroradius (Runov et al. 2009; Zhou et al. 2009a, 2011, 2017; Fu et al. 2012b; Huang et al. 2012). Recent observation have found that DFs consisted of electron-scale substructures (Liu et al. 2018c; Zhou et al. 2019). A DF is also likely a constituent of a deformed flux rope, the leading edge of which is eroded through magnetic reconnection with the geomagnetic field (Fu et al. 2013b; Wang et al. 2017; Liu et al. 2018a; Man et al. 2018).

Various types of plasma waves have been detected around the DFs. Some lower-frequency waves ($f < f_{\mathrm{lh}}$, where f_{lh} is a lower hybrid frequency), such as the magnetosonic waves and lower hybrid drift waves (LHDWs), were observed right at the front (Zhou et al. 2009a, 2014; Huang et al. 2015). Magnetosonic waves or ion Bernstein mode waves, which are probably excited by the ion ring distribution, may play crucial roles in the pre-acceleration process for electrons (Zhou et al. 2014). The LHDWs are suggested to be driven by the diamagnetic drift in the presence of a plasma pressure gradient (Davidson et al. 1977; Zhou et al. 2009a, 2009b; Chen et al. 2019). The strong LHDW can accelerate electrons in the field-aligned direction and may play important roles in the energy conversion at DF (Divin et al. 2015). On the other hand, higher-frequency waves ($f > f_{\mathrm{lh}}$) (e.g., whistler waves, electron cyclotron harmonic waves (ECH), and electrostatic emissions) are also detected around the DF (Yang et al. 2017). Whistler waves, which have frequently been observed behind the front, are believed to be generated by electron temperature or pitch angle anisotropy due to betatron acceleration (Deng et al. 2010; Fu et al. 2011, 2012c, 2013a, 2014, 2019; Khotyaintsev et al. 2011; Huang et al. 2012; Panov et al. 2013; Zhou et al. 2013; Li et al. 2015; Breuillard et al. 2016; Xu et al. 2018). Moreover, ECH waves are probably excited by the positive slope of electron perpendicular velocity distribution (Zhou et al. 2009a). ECH waves are linked to the driver of diffuse auroras (Zhang & Angelopoulos 2014), while whistler waves are likely responsible for pulsating auroras (Nishimura et al. 2010), as well as the loss and acceleration of electrons behind the DF (Panov et al. 2013). In addition, nonlinear waves, such as the electrostatic solitary waves (ESWs) and double layers, were observed at the DF (Deng et al. 2010). In summary, these kinetic waves around DFs significantly modify the particle velocity distributions and may be essential in electromagnetic energy conversion.

The aforementioned studies are related to DFs in the central plasma sheet. However, recent studies suggest that waves related to DF also occur out of equator (Pritchett et al. 2014; Le Contel et al. 2017; Zhang et al. 2017). These waves can potentially contribute to the energy dissipation out of the equator by reducing the field-aligned currents (Birn & Hesse 2005). Therefore, the study of DF deserves to be extended to the regions farther from the magnetic equator where the influence of the field-aligned currents can introduce different mechanisms and instabilities, such as the electron–electron beam instabilities with two or more components and those that are current-driven like Buneman instabilities (Le Contel et al. 2017).

In this paper, we show three different types of waves at an off-equatorial DF observed by Magnetospheric Multiscale (MMS) satellites. The remainder of this paper is organized as follows. In Section 2, we present the MMS observation of the

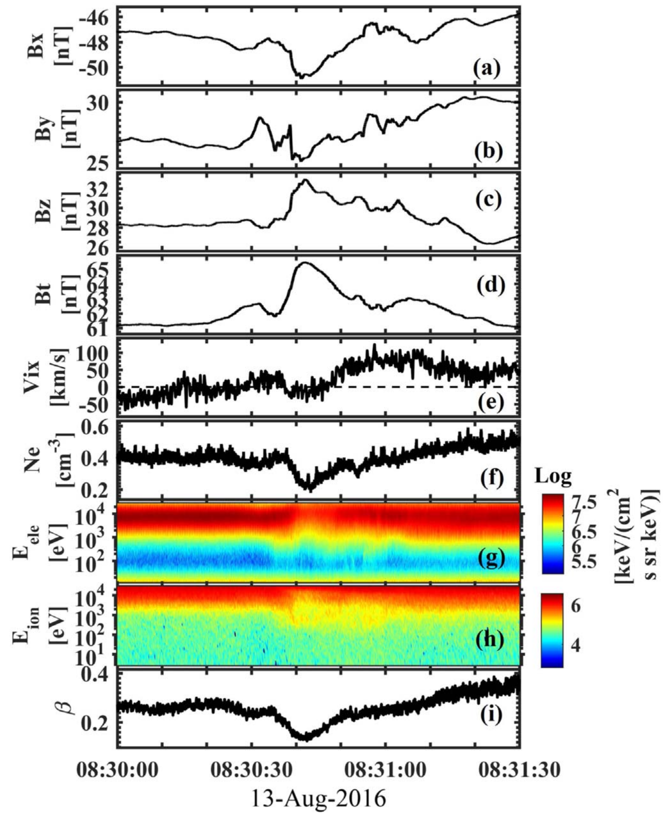

Figure 1. Overview of the DF event observed by MMS1 from 08:30:33 UT to 08:30:43 UT on 2016 August 13. Shown from top to bottom: (a) magnetic field component B_x; (b) B_y; (c) B_z; (d) total magnetic field B_t; (e) ion velocity component V_{ix}; (f) electron densities N_e; (g) omnidirectional differential energy fluxes of the 0.01–30 keV electrons and (h) 0.01–30 keV ions; (i) ion plasma beta β.

off-equatorial DF on 2016 August 13. In Section 3, the associated wave activities are analyzed. In Section 4, the electron distributions relevant to the DF and wave activities are exhibited in detail. The results are discussed and concluded in Sections 5 and 6, respectively.

2. Observations

Observational data used in this study are from the MMS mission (Burch et al. 2016). Specifically, the magnetic field data with a sampling rate of 128 Hz are from the Flux Gate Magnetometer (Russell et al. 2016); the particle data with 30 ms resolution for electrons and 150 ms for ions are from the Fast Plasma Investigation instrument (Pollock et al. 2016); DC-coupled electric field data with a sampling rate of 8192 Hz are from the Electric Double Probes (Ergun et al. 2016; Lindqvist et al. 2016; Torbert et al. 2016); and the AC magnetic field data with a sampling rate of 8192 Hz are from the search coil magnetometer (SCM; Le Contel et al. 2016). Throughout the paper, the Geocentric Solar Magnetospheric (GSM) coordinate system is used unless stated otherwise.

Figure 1 is an overview of the DF observed by MMS1 from 08:30:33 UT to 08:30:43 UT on 2016 August 13, when the satellite was at [−7.7, 3.8, −1.4] Re with satellite separations of ∼45 km. During this period, the ion plasma β is smaller than 0.5 (shown Figure 1(i)), indicating that the satellite was away from the central plasma sheet. Similar to the DF in the central plasma sheet, this DF was characterized by a rapid increase of the magnetic field B_z component (from 28 to 32.5 nT), a clear magnetic dip in B_z preceding the enhancement, and a decrease in the plasma density behind the front (Runov et al. 2009; Xu et al. 2019; Zhao et al. 2019). In this event, there was a flow deflection at 08:30:37 UT (Liu et al. 2017), when the ion plasma velocity V_x varied from $V_x \sim 50\,\mathrm{km\ s^{-1}}$ to $V_x \sim -25\,\mathrm{km\ s^{-1}}$ (see Figure 1(e)). The normal direction of the DF is $n = [-0.64, -0.48, -0.60]$, which is obtained by using the timing analysis (Harvey 1998). The moving speed of the DF along the normal is about $33\,\mathrm{km\,s^{-1}}$, embedded inside the plasma flows. Thus, the thickness of the DF is about 214 km, which is 1.5 times the local ion gyroradius ($r_{\rm gi} \sim 141$ km).

3. Wave Analysis

Electric and magnetic fluctuations (significant enhancements between 08:30:37.6 UT and 08:30:39.7 UT, marked by the white rectangles in Figure 2(b)–(c)) were observed near the ion cyclotron frequency ($f_{\rm ci}$) right at the DF. The polarization properties of the waves are shown in Figure 2. The polarization analysis is done by the singular value decomposition method (Santolík et al. 2003), which resolves the ellipticity (Figure 2(d)), wave angle (Figure 2(e)), planarity (Figure 2(f)), and the parallel Poynting flux (Figure 2(g)). The fluctuation with the planarity near 1 (red in Figure 2(f)) propagated quasi-parallel with respect to the ambient magnetic field (the wave angle is smaller than 30°, as shown in Figure 2(e)) and was primarily linearly polarized (blue in Figure 2(d)). The linear polarization of the EMIC waves in the magnetosphere was reported by Anderson et al. (1992) and Yuan et al. (2016). However, the reason for this linear polarization's occurrence is still a matter of debate. In this article, it is not a key point, so the problem of linear polarization will be not discussed in detail. Above, the wave is consistent with the characteristics of EMIC (Yu et al. 2015, 2016) and the parallel Poynting fluxes reveal that the spacecraft may have passed the source region of this wave. The parallel Poynting fluxes of these waves are primarily positive (see Figure 2(g)), indicating that they propagated parallel to the ambient magnetic field. Because the spacecraft was in the southern hemisphere during this interval ($B_x < 0$), the EMIC waves propagated toward the plasma sheet. The parallel Poynting fluxes change from positive to negative at 08:30:38.5 UT, further implying that the spacecraft may occasionally pass the source region of the EMIC waves—that is to say, the DF could be the source region of the EMIC waves in this event.

It is interesting that other wave activity below the lower hybrid frequency and above the ion cyclotron frequency was detected by MMS from 08:30:39.4 UT to 08:30:39.9 UT, as shown in Figure 3. This activity propagated highly oblique to the ambient magnetic field. More details of this fluctuation are displayed in Figure 4, including the corresponding waveforms of the magnetic and electric field in field-aligned coordinates (FAC) by filtering the MMS data with a bandpass filter around $f_{\rm lh}$ (between 10 and 100 Hz), the controlling parameter of density gradient $L_n/r_{\rm gi}$ (L_n is the density gradient length scale and $r_{\rm gi}$ is the ion gyroradius), and the scalar potentials calculated from the electric and magnetic fields. The electric field perturbation (δE) of this wave is predominantly in the direction perpendicular to B_0, while magnetic field perturbation (δB) was primarily in the parallel direction (shown in Figure 4(a) and (b)). These features are similar to the properties

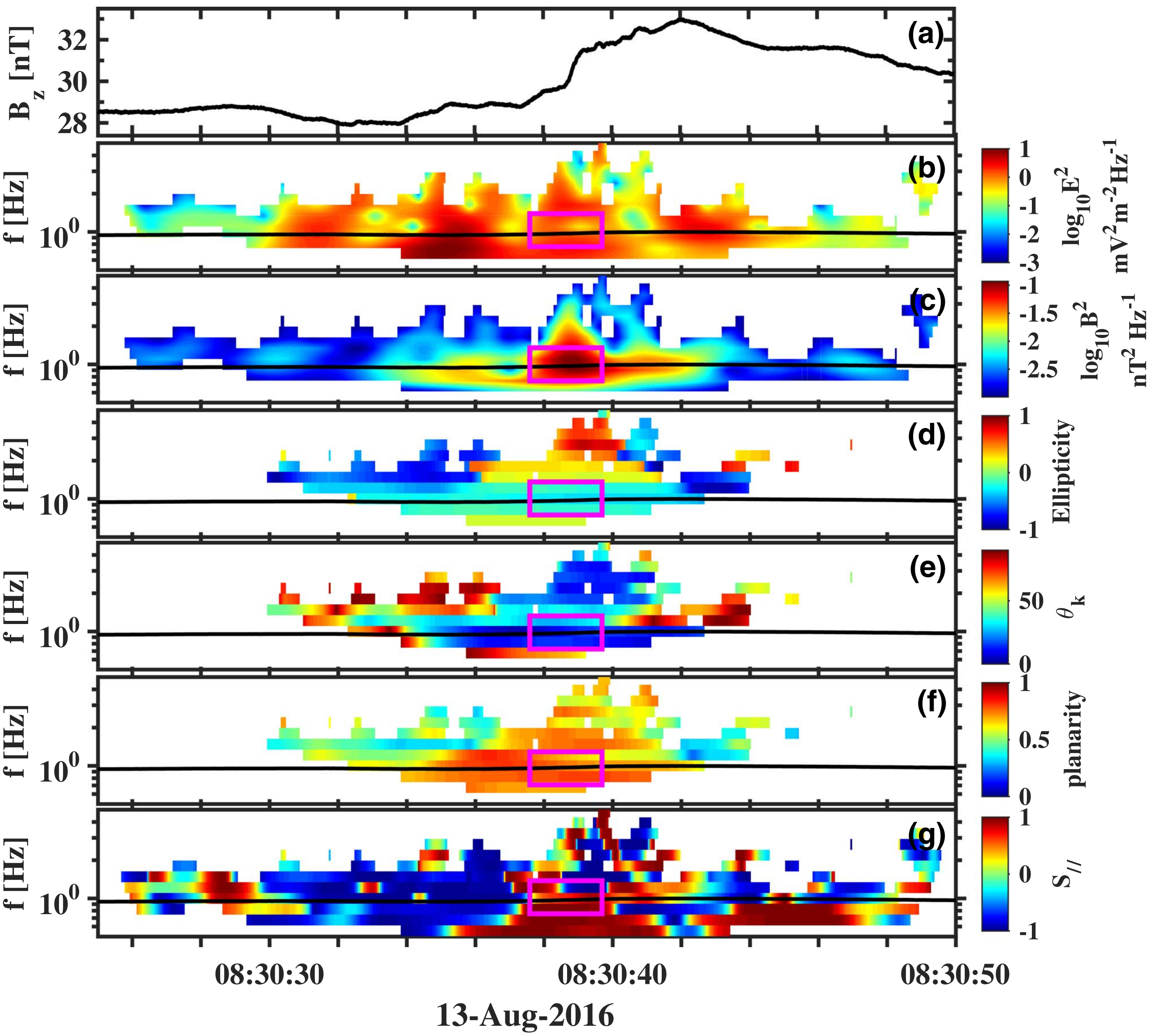

Figure 2. Wave polarization analysis. Shown from top to bottom: (a) magnetic field component B_z; (b) and (c) E and B spectrograms; (d) ellipticity (+1 denotes the right-handed circular polarization and −1 denotes the left-handed circular polarization); (e) propagation angle; (f) planarity; (g) parallel Poynting flux (positive values indicate propagation parallel to the magnetic field and negative values indicate propagation antiparallel to the magnetic field). Black lines in panels (b)–(g) indicate ion gyro-frequency $f_{\rm ci}$. Wave is marked by the magenta rectangle.

of LHDW observed in the magnetotail (Zhou et al. 2009b, 2011). In order to determine whether the wave was either predominantly an electrostatic or an electromagnetic wave, we estimated the value of $|\delta E/\delta B|$. The value reaches 5×10^8 km s^{-1}, which is much greater than all the local characteristic speeds, such as the Alfvén speed and the diamagnetic drift speed. Thus, it is unlikely that this wave is electromagnetic. To excite the LHDI, sharp density gradients are needed, which leads to the condition $L_n/r_{\rm gi} < (m_i/m_e)^{1/4} = 6.5$ (Huba et al. 1978). The density gradient is also related to the diamagnetic drift through $L_n/r_{\rm gi} = V_{\rm thi}/(2V_{\rm Di})$, where $V_{\rm thi}$ is the ion thermal velocity and $\boldsymbol{V}_{\rm Di} = \boldsymbol{V}_{\perp i} - \boldsymbol{E} \times \boldsymbol{B}/B^2$ is the ion diamagnetic drift velocity. During the time period considered in Figure 3, large density gradients are present (Figure 1(f)). According to the ratio of $V_{\rm thi}$ and $V_{\rm Di}$, the $L_n/r_{\rm gi}$ is obtained (shown in Figure 4(c)). Corresponding to the time period of fluctuation, $L_n/r_{\rm gi} \sim 1$ indicates that the density gradient is sharp. Another interesting feature of the electrostatic LHDW is that the perpendicular electric field perturbation induces perturbations in the parallel magnetic field component through the current carried by electrons with $\delta\boldsymbol{E} \times \boldsymbol{B}_0$ drift. Adopting the method introduced by Norgren et al. (2012) and used by Le Contel et al. (2017) and Zhou et al. (2014, 2018), we analyzed this plasma wave with $f_{ci} \ll f \sim f_{\rm lh} \ll f_{\rm ce}$ (where $f_{\rm ce}$ is electron gyrofrequency), since ions are unmagnetized on lower hybrid timescales and only electrons carry a current. At this short timescale, that ions are assumed to be stationary. The wave perpendicular current can be obtained from the electron electric drift as $-en_e(\delta\boldsymbol{E} \times \boldsymbol{B}_0)/B_0^2$, where e is the electron charge and n_e is the electron density. According to Ampèrés law and assuming a quasi-electrostatic field, the electrostatic potential can be estimated form the magnetic field and electron density as $\delta\phi = B_0\delta B_{/\!/}/(en_e\mu_0)$, where $\delta\phi$ is the electrostatic potential, $\delta B_{/\!/}$ is the parallel magnetic field fluctuation, and μ_0 is the free space magnetic permeability. On the other hand, the electrostatic potential can be directly obtained by integrating

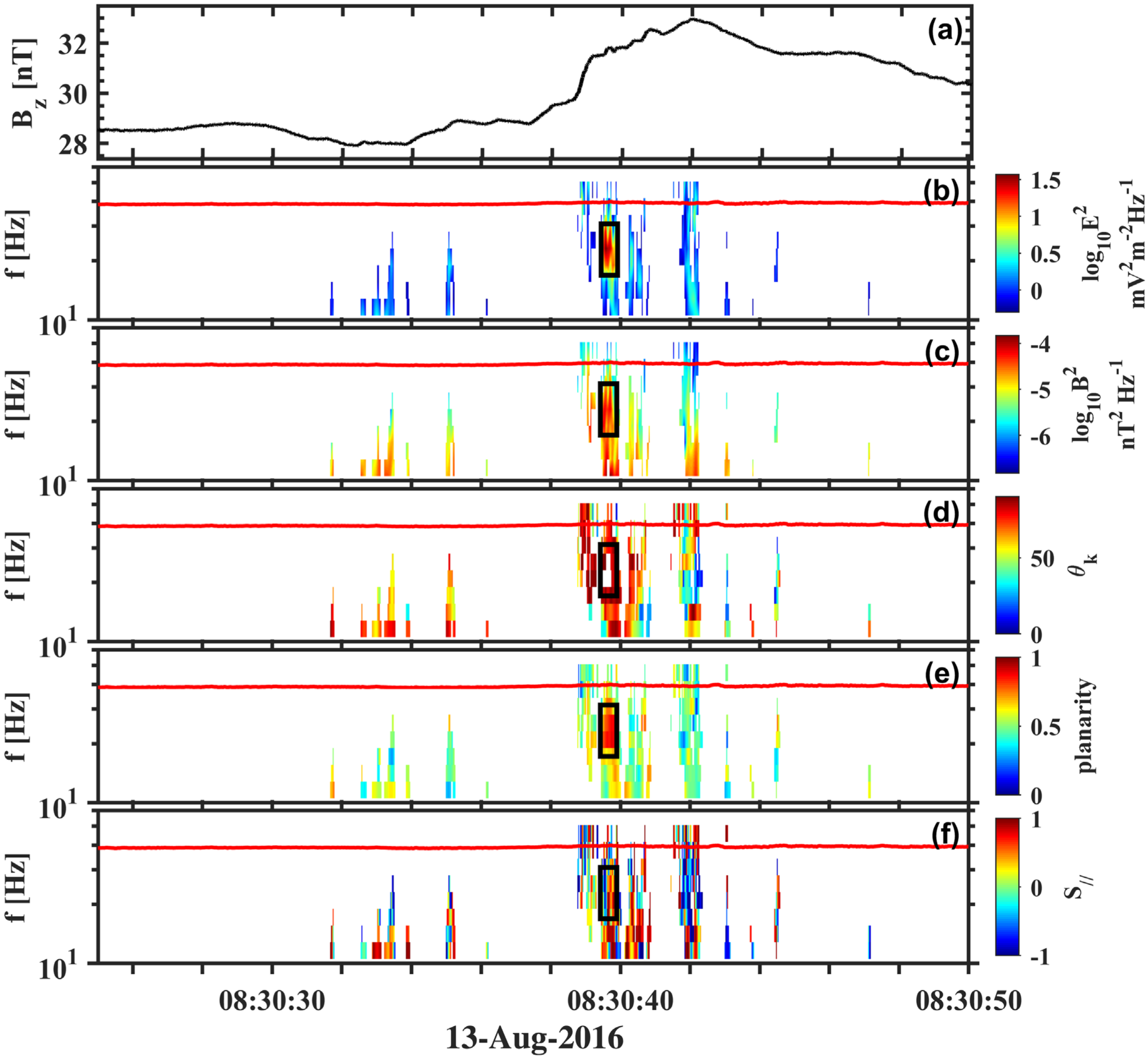

Figure 3. Wave polarization analysis. From top to bottom: (a) magnetic field component B_z; (b) and (c) E and B spectrograms; (d) propagation angle; (e) planarity; and (f) parallel Poynting flux (positive values indicate propagation parallel to the magnetic field and negative values indicate propagation antiparallel to the magnetic field). Red lines in panels (b)–(f) indicate ion lower hybrid frequency f_{lh}. Wave is marked by the black rectangle.

the perpendicular electric field (which is the dominant component) along the direction of the propagation $\delta\phi = \int \delta E_{\perp} \cdot \nu_{\mathrm{ph}} dt$, where ν_{ph} is the phase speed. We have surveyed the ν_{ph} in a given amplitude range and in all possible directions to find the optimal solution of ν_{ph}. A good agreement between the electric and magnetic potentials is exhibited in Figure 4(d). The best match between the two calculations of the electrostatic potential provides a good estimation of the wave phase velocity ν_{ph}. Table 1 shows the results of this analysis for the MMS1 satellite between 08:30:39.4 and 08:30:39.9UT. It shows that the fluctuation had a frequency close to f_{lh} (about 40 Hz) and propagated perpendicular to $\boldsymbol{B}$ with a phase speed about 190 km s^{-1}. The corresponding wavelength is 12 km $\sim 0.1 r_{\mathrm{gi}}$ and $k\rho_e \sim 0.9$ (ρ_e is the electron gyroradius). All these properties confirm that the fluctuation was LHDW.

Large-amplitude nonlinear ESWs were also observed at the DF, between 08:30:41 UT and 08:30:42 UT, which is about 1 s after the LHDW was detected by MMS1. The expanded panel of the field-aligned and perpendicular electric field components between 08:30:41.58 UT and 08:30:41.68 UT are shown in Figure 5(d) and (e), respectively. It clearly shows a train of solitary bipolar pulses in the electric field parallel to the background field and unipolar electric field perpendicular to the background field. All of these structures have positive–negative polarity in $\delta E_{//}$ signals (shown in Figure 5(d)), indicating they are traveling in the same direction and are likely from the same source. Amplitudes of parallel electric field and perpendicular electric field are comparable. The average amplitudes of the parallel and perpendicular components of the ESWs are $\sim$40 mV m^{-1}, which are well above the measurement uncertainty (about 2 mV m^{-1} in this period). The electric field features are similar with the ones of multidimensional electron hole (EH) structures described by Mozer et al. (2015). The perpendicular electric field feature was explained as the combined actions between the transverse instability and stabilization by the background magnetic field (Lu et al.

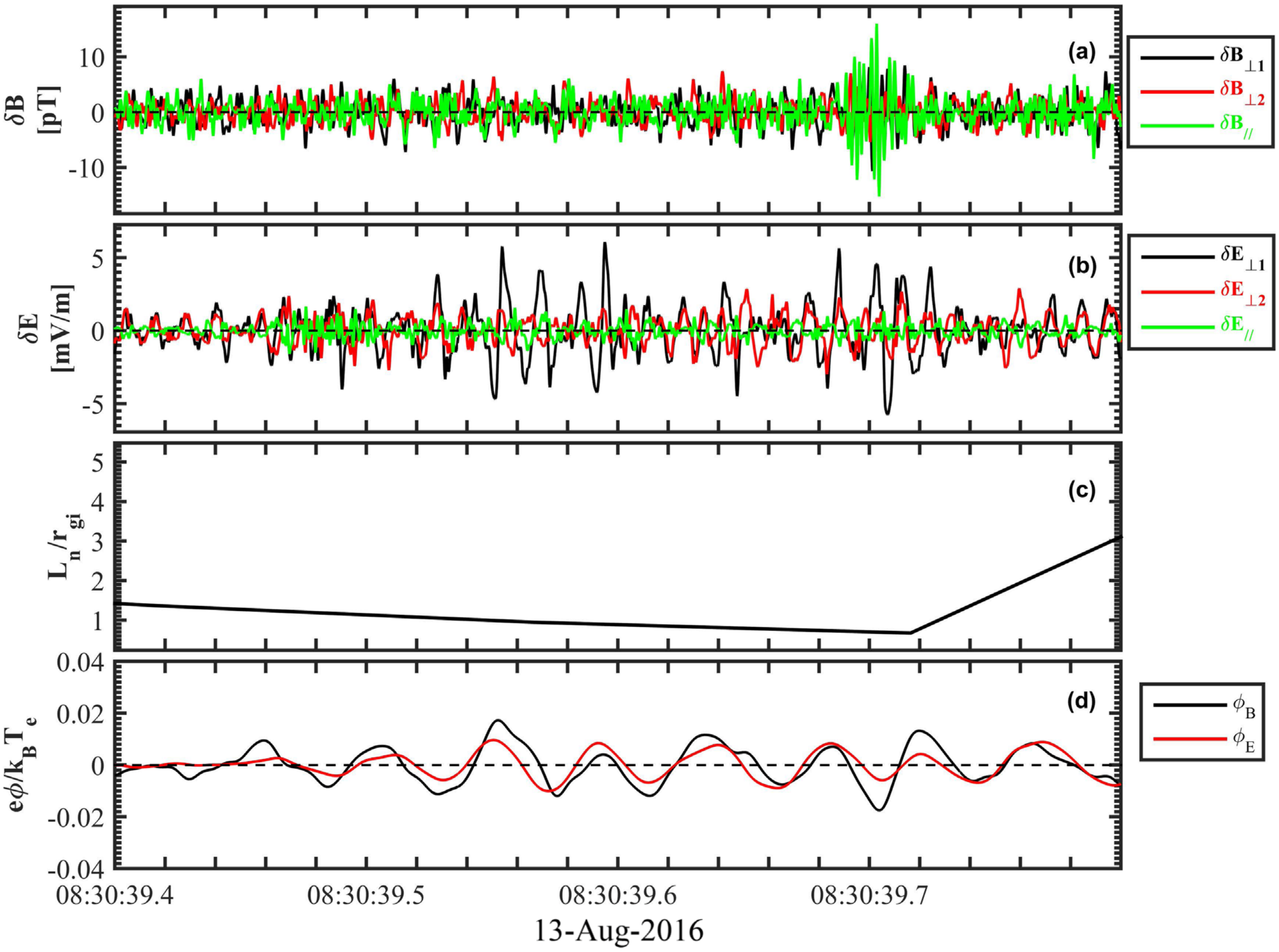

Figure 4. More details of the fluctuation in Figure 3. From top to bottom: (a) magnetic field waveform in FACs illustrated by filtering the MMS data with a bandpass filter around $f_{\rm lh}$ (between 10 and 100 Hz); (b) electric field waveform in FACs illustrated by filtering the MMS data with a bandpass filter around $f_{\rm lh}$ (between 10 and 100 Hz); (c) controlling parameter of density gradient $L_{\rm n}/r_{\rm gi}$; (d) scalar potentials calculated from the electric and magnetic fields.

Table 1
Properties of the Electrostatic Potential Fluctuations for MMS1 Satellite Between 08:30:39.4 and 08:30:39.9 UT

Satellite	f(Hz)	$v_{\rm ph}$(km s^{-1}) in GSM	$k\rho_e$	$\delta\phi/T_e$
MMS1	15–30	$190 * [-0.29, 0.93, -0.20]$	0.9	0.01

2008) or the wave-particle interactions inside the ESW (Fu et al. 2020). Recently, magnetic field perturbation features of the multidimensional, electromagnetic EHs were reported by Andersson et al. (2009) and Vasko et al. (2015). The magnetic field perturbation ($\delta B_{//}$) parallel to the ambient magnetic field is positive unipolar with amplitudes about 10–100 pT. The δE_x (the electric field perturbation perpendicular to the ambient magnetic field) and δB_y (the magnetic field perturbation perpendicular to the ambient magnetic field) signals are correlated, while the δE_y (the another electric field perturbation perpendicular to the ambient magnetic field) and δB_x (the other magnetic field perturbation perpendicular to the ambient magnetic field) signals are anticorrelated. These features of magnetic field perturbations are obviously detected by MMS2. The high-time resolution $\delta \boldsymbol{E}$ and $\delta \boldsymbol{B}$ signals observed by MMS2 between 08:30:41.20 UT and 08:30:41.30 UT are displayed in Figure 6. The signals are plotted in the FAC system such that the subscript // indicates the direction parallel to the ambient magnetic field, and the x and y components are perpendicular to the ambient magnetic field. The $\delta E_{//}$ signals show a series of bipolar structures and the identical positive–negative polarities. In addition, these structures have positive, unipolar $\delta B_{//}$ signals with amplitudes up to $\sim$15 pT, as displayed in Figure 6(b). Panels (c)–(f) of Figure 6 show that the δE_x and δB_y signals are correlated while the δE_y and δB_x signals are anticorrelated for these structures. The above-mentioned features of electric and magnetic fields are coincident with the observation features of EHs reported by Andersson et al. (2009). The magnetic field signals were interpreted as the Lorentz transformation of the perpendicular electric fields of a rapidly moving electrostatic EH. Thus, a simplified Lorentz transformation is introduced to derive the velocity ($\nu_{\rm EH}$) of the electromagnetic EHs. According to the equation $\delta B_y = \nu_{\rm EH}\delta E_x/c^2$, the derived velocity $\nu_{\rm EH}$ is about 5×10^4 km s^{-1}, which is larger than the electron thermal velocity (about 2×10^4 km s^{-1}). Using the derived velocity, the size of the EHs along the ambient magnetic field ($L_{//}$, the distance between the negative and positive peaks in $\delta E_{//}$) is roughly $14\lambda_D$ (λ_D is electron Debye length, about 5 km) and the average positive potential Φ is about 2 kV ($e\Phi/K_{\rm B}T_e \sim 0.7$). Above all, the detected ESWs are indeed multidimensional, electromagnetic EHs with a significant positive central potential, suggesting strongly nonlinear behavior.

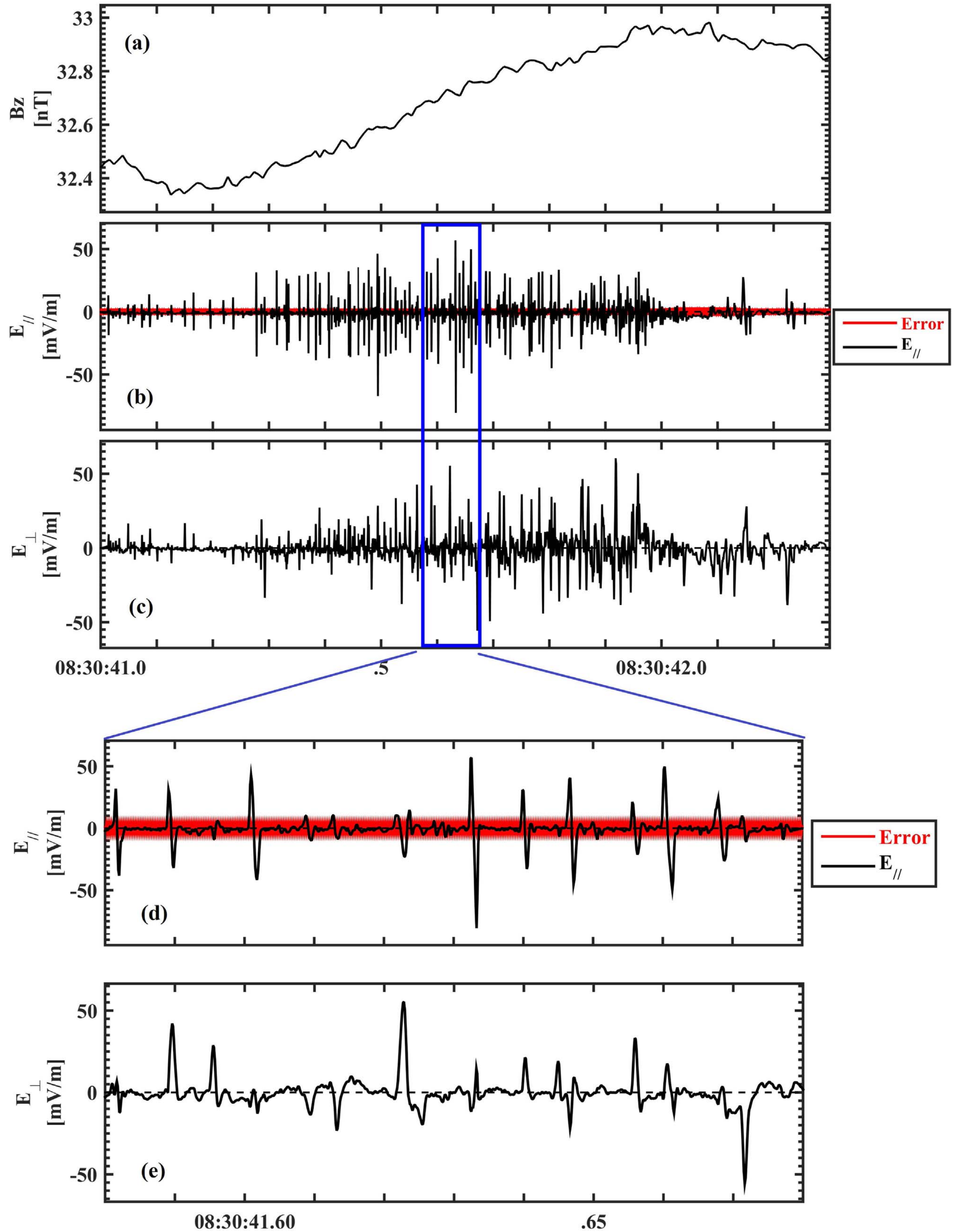

Figure 5. ESWs observations by MMS1. From top to bottom: (a) magnetic field component Bz; (b) parallel electric field (black) and its error bar (red); (c) perpendicular electric field; (d) expanded parallel electric field (black) and its error (red) between 08:30:41.58 UT and 08:30:41.68 UT; (e) expanded perpendicular electric field between 08:30:41.58 UT and 08:30:41.68 UT.

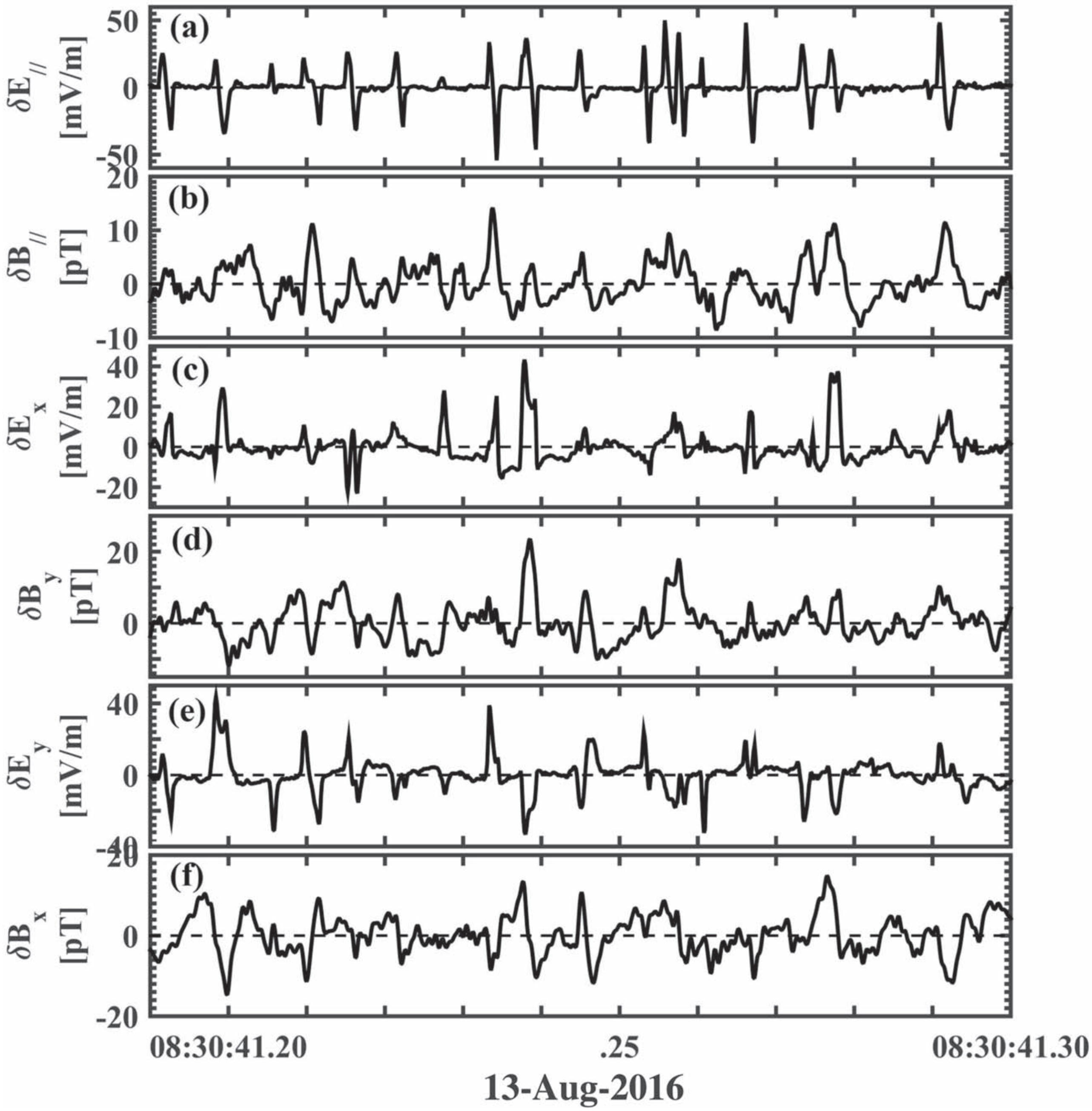

Figure 6. Electric and magnetic field perturbations in ESWs observations between 08:30:41.20 UT and 08:30:41.20 UT by MMS2. Data are plotted in the FAC system. In panels (a) and (b), subscript // indicates that the corresponding component is parallel to the ambient magnetic field, and the x and y components are perpendicular to the ambient magnetic field. From top to bottom: (a) $\delta E_{//}$, (b) $\delta B_{//}$, (c) δE_x, (d) δB_y, (e) δE_y, and (f) δB_x.

4. Electron Dynamics

As shown in Figure 7, the electron fluxes associated with different subregions of DF have different behaviors (see Figure 7(c)–(e)). It is obvious that, corresponding to time b (EMIC waves), the antiparallel and perpendicular electron fluxes at the energy range of about 0.3–2 keV become strong (displayed in Figure 7(d) and (e)). When the spacecraft encountered the DF, the energetic electron flux between 24 and 58 keV started to increase (shown in Figure 7(f)). The detailed pitch angle distributions relevant to the DF are shown in Figure 8 for four different time instants (marked by the four vertical lines in Figure 7(a)).

In Figure 7(a) time a corresponds to the ahead of the DF, time b corresponds to the EMIC waves, time c corresponds to the LHDW, and time d corresponds to the ESWs, respectively. Figure 8(a) shows that the enhancement of energetic electrons fluxes ahead of the DF appears mainly in the parallel and antiparallel directions. This is a typical cigar distribution (Baker et al. 1978) and is usually attributed to Fermi acceleration (Fu et al. 2011). Another interesting point is that we see a net antiparallel drift for electrons in the energy range of about 0.3–2 keV, by comparing the antiparallel and parallel electron phase space density (PSD) in Figure 8(a)–(d). The antiparallel drifting electrons are probably responsible for the parallel current at the front. The relation between the electron drift and the observed EMIC waves is further analyzed in detail in the

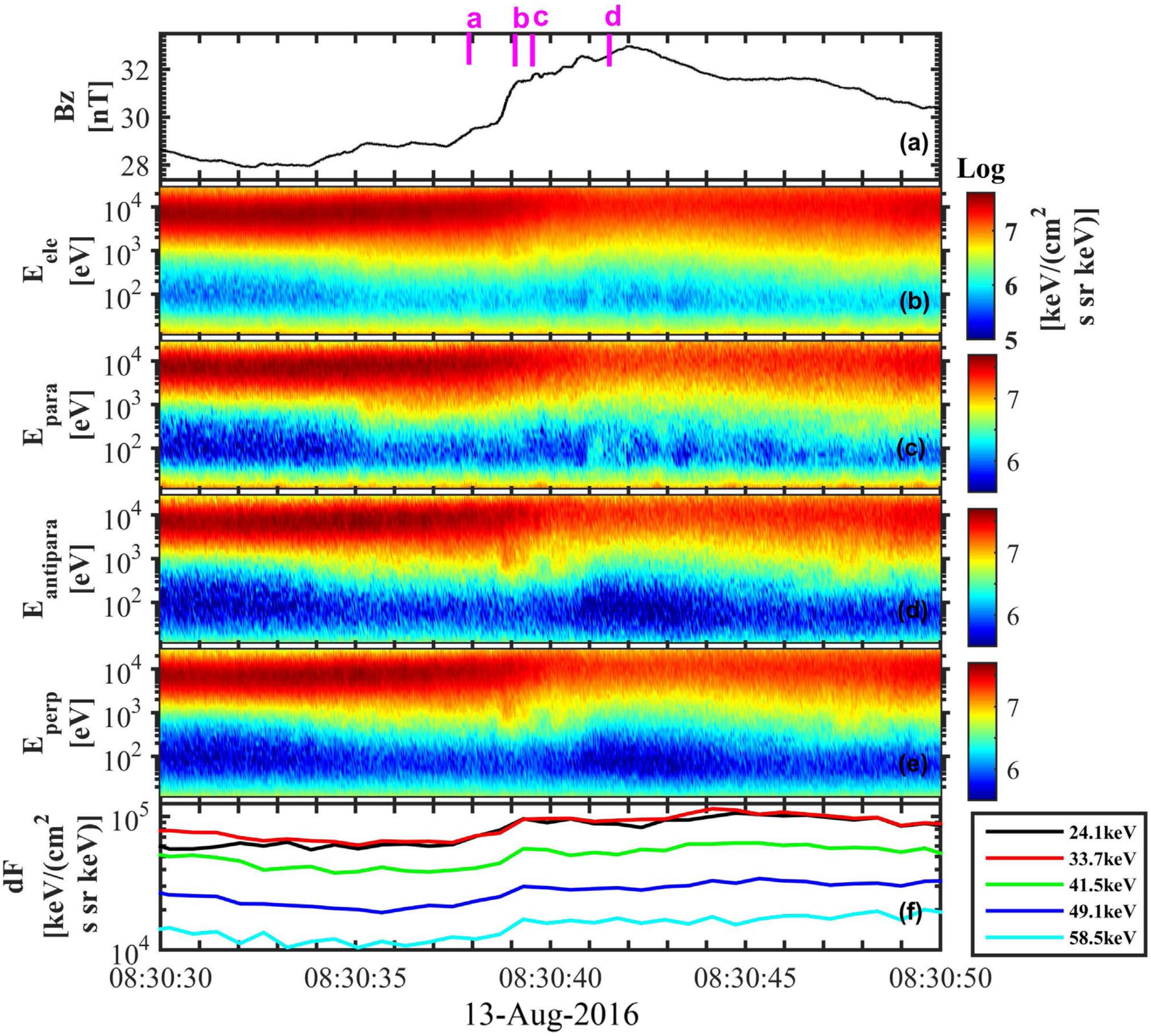

Figure 7. Electron distribution. From top to bottom: (a) magnetic field component Bz; (b) omnidirectional differential fluxes; (c) parallel fluxes; (d) antiparallel fluxes; (e) perpendicular fluxes of the 0.01–30 keV electrons; and (f) electron differential fluxes. Short vertical magenta bars mark the four different time instants when the electron distributions are shown in Figure 8.

next section. Corresponding to the time (c), the drift between antiparallel and parallel electron becomes weak. It may originate from the parallel heating of electrons by LHDI wave. When at time (d), the electron PSD in the field-aligned direction is larger in comparison with antiparallel and perpendicular PSDs. ESWs can be the possible energy sources for accelerating electrons in the parallel direction.

5. Discussion

In the following, we discuss the generation mechanism of the EMIC waves. Figure 8 shows the B_z component (Figure 9(a)), the current density in the field-aligned coordinate (FAC) (Figure 9(b)), the values of $|\nabla \cdot \boldsymbol{B}|/|\nabla \times \boldsymbol{B}|$ (Figure 9(c)), the sum of the ion current density and electron current density in the FAC (Figure 9(d)), the ion current density (Figure 9(e)), and the electron current density in FAC (Figure 9(f)), respectively. The current density shown in Figure 9(b) was calculated by using the curlometer technique (Dunlop et al. 2002). The ratio of $|\nabla \cdot \boldsymbol{B}|/|\nabla \times \boldsymbol{B}|$ indicates the computational reliability of the curlometer method. We see that the estimated current densities in the period corresponding to ion cyclotron waves are reliable because the values of $|\nabla \cdot \boldsymbol{B}|/|\nabla \times \boldsymbol{B}|$ are small (Figure 9(c)). There was a strong parallel current (about 60 nA m^{-2}) corresponding to the EMIC waves. At the corresponding time period, the sum of ion current density and electron current density is nearly equal to the current density estimated by the curlometer method. We also compare the ion current with the electron current (Figure 9(e) and (f)) and find that the main carrier of the parallel current is electron. This means that the electrons drifting in the antiparallel direction produce the parallel current.

Furthermore, we calculated the linear dispersion relation of the waves and the associated growth rate by using the Waves in Homogeneous Anisotropic Multicomponent Plasma (WHAMP) code (Rönnmark 1982). A model comprised of Maxwellian distribution functions is used to fit the input parameter of WHAMP. Background magnetic field strength

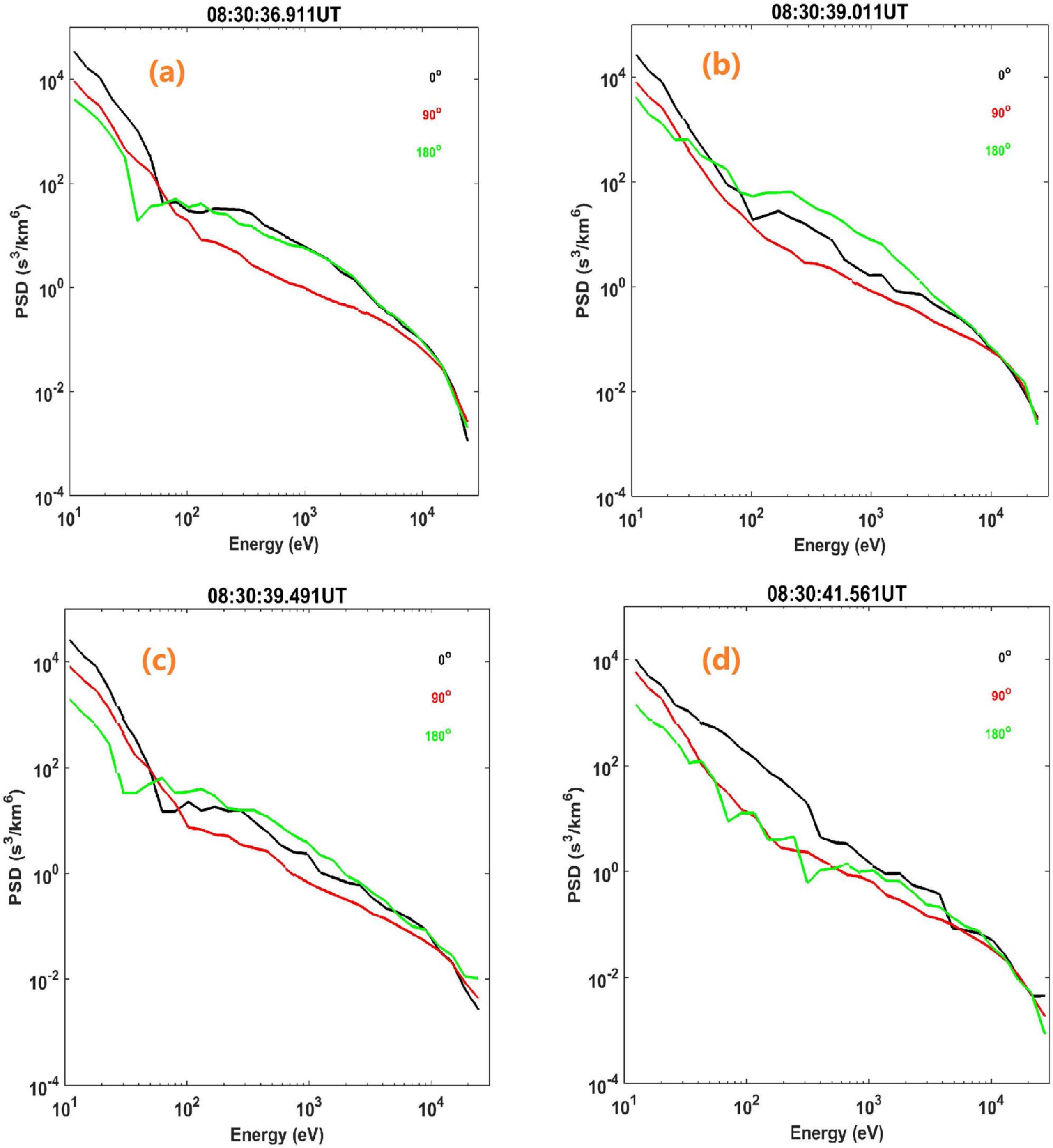

Figure 8. Electron pitch angle distributions detected by MMS1 for four different time instants denoted in Figure 6. Color curves indicate the PSD at different pitch angles: 0° (black), 90° (red), and 180° (green).

and ion temperature are set as $B_0 = 63$ nT; $T_i = 2500$ eV. We assume that the electrons consisted of three populations: one cold component with no drift and a lower number density ($n = 0.09\ \mathrm{cm}^{-3}$; $T = 100$ eV), one cold component with antiparallel drift and a lower number density ($n = 0.09\ \mathrm{cm}^{-3}$; $T = 230$ eV; $V_d = -6000\ \mathrm{km\ s}^{-1}$, where V_d is the drift velocity between the antiparallel electrons and parallel electrons), and one hot component with no drift and a higher number density ($n = 0.2\ \mathrm{cm}^{-3}$; $T = 4000$ eV). Figure 10(a) compares the fitted three-population electron distribution. The black dashed line denotes a cold component with no drift and lower number density; the green solid line denotes a cold component with antiparallel drift and a lower number density; the black solid line denotes a hot component with no drift and a higher number density. The observed electron distribution at two different pitch angles (0° and 180°) are marked by circles. We see that the fitting results (thick lines) quantitatively agree with the spacecraft observations. The drift velocity from our fitting result is $0.24\ V_{e,\mathrm{th}} \sim 6000\ \mathrm{km\ s}^{-1}$ ($V_{e,\mathrm{th}}$ is the electron thermal velocity, about $2.5 \times 10^4\ \mathrm{km\ s}^{-1}$). Figure 10 exhibits the dispersion relation (black line) and the growth rate of the $\theta_k = 10°$ branch (red line). The growth rate is positive,

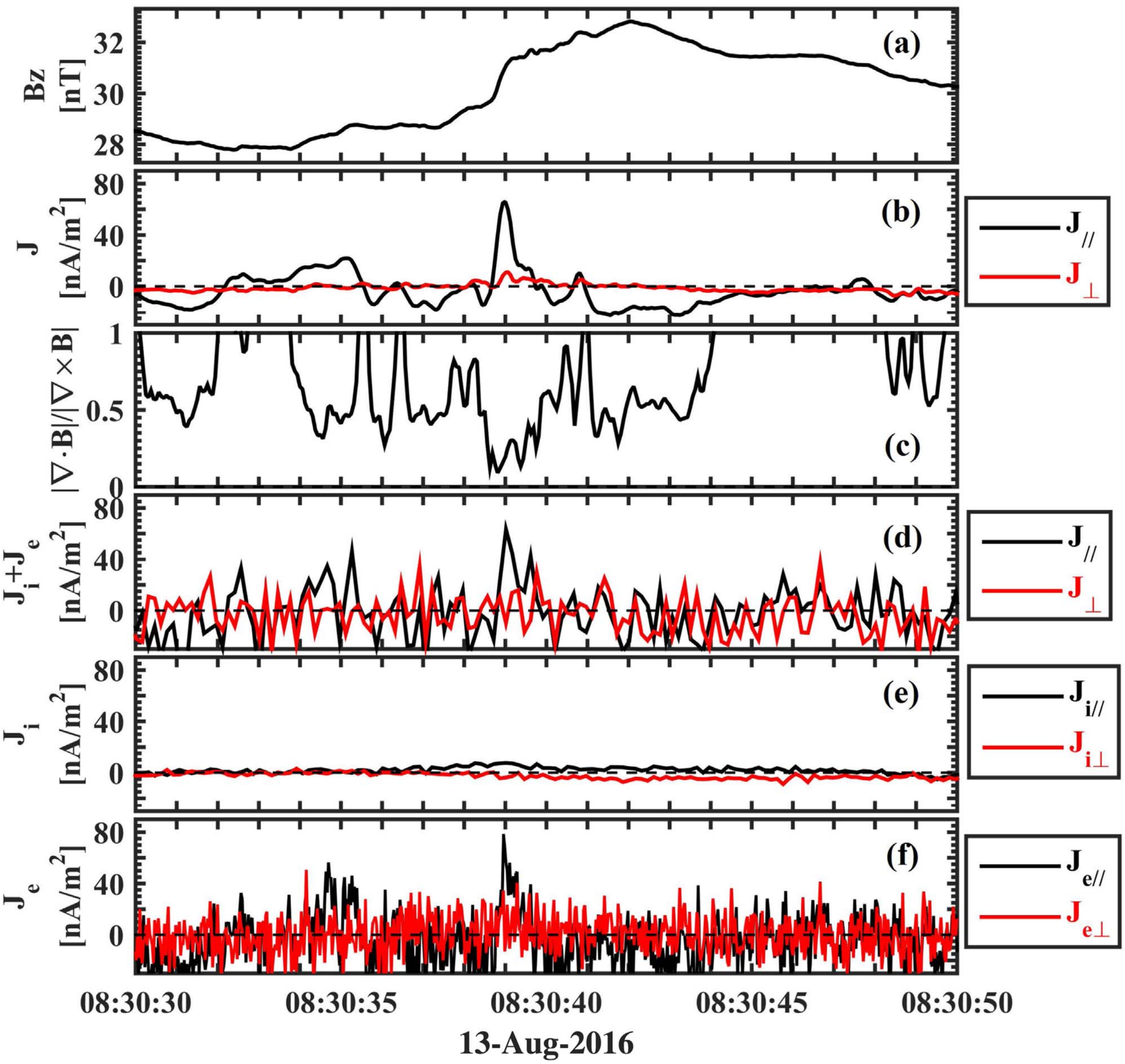

Figure 9. Current densities. From top to bottom: (a) magnetic field component B_z; (b) current density calculated by curlometer method in FAC coordinates; (c) values of $|\nabla \cdot \boldsymbol{B}|/|\nabla \times \boldsymbol{B}|$; (d)–(f) the sum of ion current density, the ion current density, and the electron current density in FAC coordinate, respectively. The color curves in panels (b) and (d)–(f) indicate the parallel (black) and perpendicular (red) components, respectively.

meaning that the wave can be generated in the local plasma environment. The maximum growth rate $\gamma = 0.98\Omega_{\text{ci}}$ (Ω_{ci} is ion gyrofrequency) is found at $\omega = 0.98\Omega_{\text{ci}}$ in the dispersion relation (black line), which is consistent with the observed frequency of the ion cyclotron wave in this event. The wave phase velocity V_{ph} is about 3000 km s^{-1} $\sim 1.6V_{\text{A}}$, where V_{A} is the Alfvén speed, which is approximately in accordance with the estimated phase speed of the ion cyclotron wave inferred ($1.5V_{\text{A}}$) by $|\boldsymbol{E}/\boldsymbol{B}|$. The result is similar to the conclusions reported by Perraut et al. (2000), i.e., for small k, the dispersion relation with oblique propagation was $\omega = k_{//}V_d/2$, where $V_d/2 = 1.5V_{\text{A}}$ in this case. However, in this case, the wave exhibits parallel propagation. Moreover, it is worth noting that $k_{//}r_{\text{gi}} < 1$ when the maximum growth rate is near Ω_{ci} in Figure 8(b). This is consistent with the results of Gary et al. (1976), which illustrated that the current-driven kink-like instability was unstable with frequency near Ω_{ci} and normalized wavevector $k_{//}r_{\text{gi}} < 1$. In addition, they predicted that the maximum growth rate $\gamma_{\max} \sim \Omega_{\text{ci}}$ should occur at $\omega \sim \Omega_{\text{ci}}$ and $k_{\max} \sim 2\Omega_{\text{ci}}/V_d$ as a result of the kink-like instability (Gary et al. 1976). According to their theory, the wavevector corresponding to the maximum growth rate $k_{\max}$ ($k_{\max}$ is normalized to ion gyroradius) was about 0.2, which is the same as that inferred from WHAMP. Consequently, we believe that the current-driven kink-like instability led to the observed EMIC waves. Since the width of the parallel current was less than the ion gyroradius, the homogenous assumption used in the WHAMP calculation may be invalid. Therefore, particle-in-cell (PIC) simulations of waves generated in an inhomogeneous magnetic field geometry is required to have a better understanding of the generation and properties of the EMIC waves observed at this thin DF.

It is not a unique event that the EMIC wave was observed at the off-equatorial DF. We found the same waves generated by

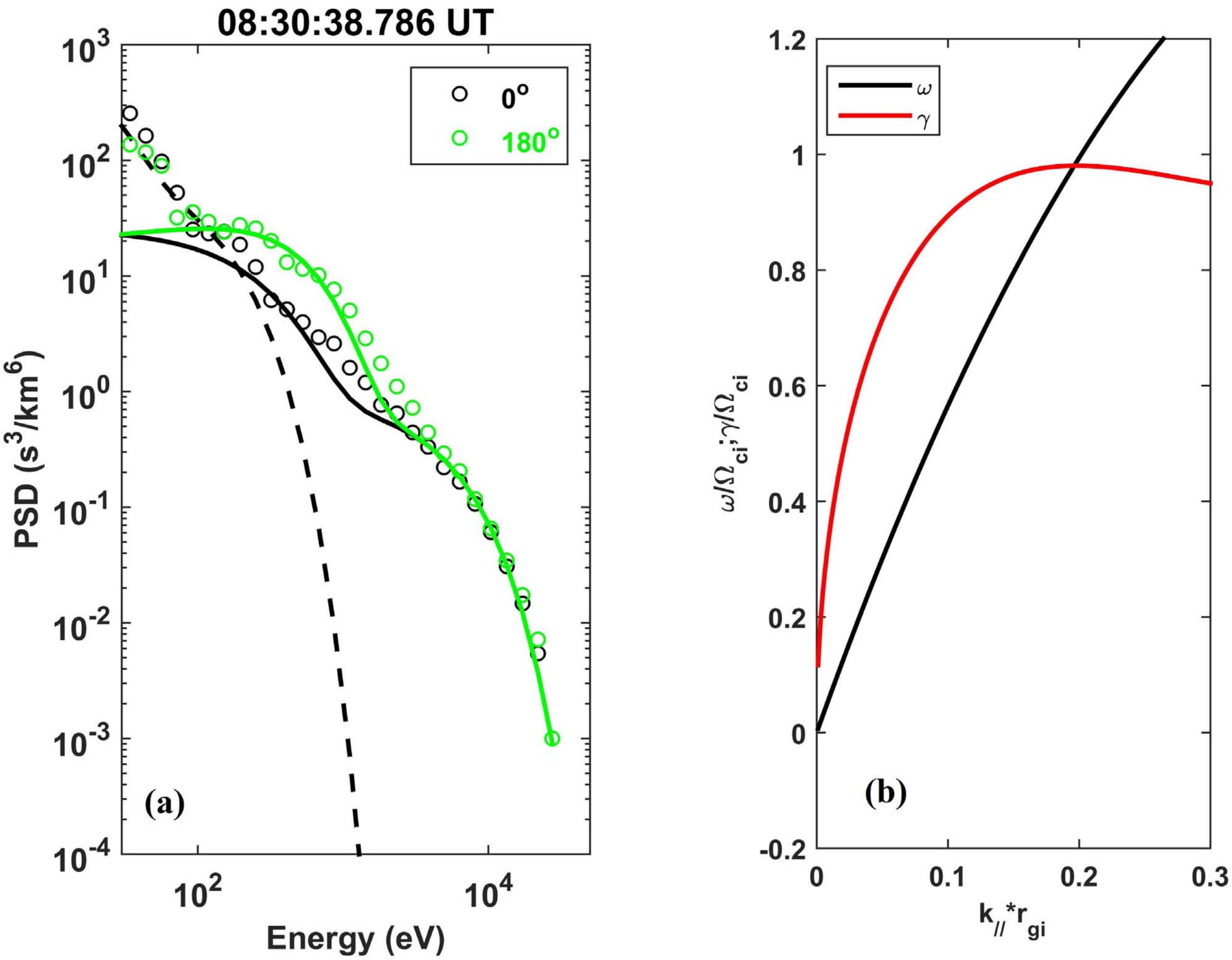

Figure 10. (a) Observed and fitted electron phase densities (PSD) at pitch angle $\theta = 0°$ (black) and 180° (green). Circles are observations. Curves are the fitting results. Black dashed line denotes one cold component with no drift and lower number density. Green solid line denotes one cold component with antiparallel drift and lower number density. Black solid line denotes one hot component with no drift and higher number density. (b) Dispersion relation (black) and growth rates (red) of the ion cyclotron modes predicted from the fitted distributions.

the current-driven kink-like instability at an off-equatorial DF observed by the MMS spacecraft on 2016 August 10 (not shown here).

Recent 3D PIC simulations and observations have found electromagnetic instabilities with frequency near the ion cyclotron frequency ahead of approaching DFs at the plasma sheet boundary layer (Pritchett et al. 2014; Zhang et al. 2017). The simulation showed that the wave propagated highly oblique to the ambient magnetic field. It is produced by the electromagnetic current-driven ion cyclotron instability as a result of a large parallel current, resulting from a net parallel drift between electrons and ions. Observations of Time History of Events and Macroscale Interactions during Substorms satellites reported two different precursor waves for an off-equatorial DF (Zhang et al. 2017). One of the waves was at about 0.3 Hz, left-hand polarized, and oblique propagated. The other one was at a much lower frequency (0.02 Hz), right-hand polarized, and parallel propagated. They also found a parallel current attributed to an electron beam coexisted with the waves. It is demonstrated that the higher-frequency instability is a current-driven ion cyclotron instability and the lower-frequency instability is a kink-like instability. However, these off-equatorial waves were observed ahead of approaching DFs, instead of at the DF layer. In this paper, we report the EMIC waves at an off-equatorial DF, which was identified by the peak frequency near the ion cyclotron frequency, linear polarization, and parallel propagation. In addition, observations of three different waves in different regions of a single DF indicate the existence of substructures of the DF.

6. Summary

Utilizing high-resolution data from the MMS spacecraft, we studied the wave characteristics and wave–particle interactions at an off-equatorial DF. Our key points are summarized below:

1. The nearly parallel propagating EMIC wave was observed at an off-equatorial DF. The wave had its peak frequency near the local proton cyclotron frequency and was linear polarized. The off-equatorial DF was probably the source region and we suggest that the wave was driven by a parallel electron current at the front.
2. Three different plasma waves associated with different electron pitch angle distributions were detected at different subregions of a single DF, which implies the existence of substructures of the DF.
3. The detected ESWs are interpreted as multidimensional electromagnetic EHs that are manifestations of several

distinguishing features in electric and magnetic field perturbation. The EHs with a significant positive central potential suggested the likelihood of strongly nonlinear behavior.

A parallel current, which resulted from the antiparallel drift of electrons at the energy range of about 0.3–2 keV, was detected during the period of EMIC waves. We confirm that the EMIC waves are generated by the current-driven kink-like instability, the free energy of which is provided by the drifting electrons. Previous works indicate that the field-aligned currents, a diversion of the perpendicular current near the equator, constitute the global current system in the magnetotail (Liang et al. 2013; Yao et al. 2016). The current-driven EMIC waves may reduce the field-aligned current by consuming the bulk kinetic energy of the electrons. Therefore, this instability has the potential to contribute to global energy dissipation. The role of this wave on the global magnetosphere–ionosphere coupling will be studied further in the future.

On the other hand, after the detection of the EMIC waves, LHDW and ESWs were observed in different subregions of this DF. About 1 s after the observation of LHDW, a train of electric solitary waves with amplitudes up to $E_{//} \sim 40\,\mathrm{mV\,m^{-1}}$ were detected. In addition, the perpendicular electric field exhibited unipolar structure while the parallel electric field exhibited bipolar structure with positive–negative polarity. Amplitudes of the parallel and perpendicular electric field components are comparable. Though the ESWs were reported at DFs in the plasma sheet by Deng et al. (2010), they did not discuss the feature in magnetic field perturbation of ESWs. In this paper, it is worth noting that the structures have several distinguishing features in magnetic field perturbation. The magnetic field perturbation ($\delta B_{//}$) parallel to the ambient magnetic field is positive unipolar with amplitudes about 15 pT. The perpendicular components δE_x and δB_y are correlated, while the perpendicular components δE_y and δB_x are anticorrelated. A simplified Lorentz transformation has been introduced to obtain the velocities of EHs, which are larger than the electron thermal velocity. We have demonstrated that the ESWs have a size on the order of one Debye length, as well as positive potentials. These features are consistent with those of the multidimensional electromagnetic EHs. As we know, the transition between one-dimensional and multidimensional structure is likely related to the generation of lower hybrid waves or electrostatic whistler waves (Umeda et al. 2006). The observation of multidimensional EHs at the DF implies a more complex wave–particle interaction at the DF than that found in Deng et al. (2010). However, the certain interaction between LHDW and ESWs at the DF layer remains unknown. More theoretical and observational investigations are needed to clarify the interaction associated with DF structure out of the equator.

This work is supported by the National Natural Science Foundation of China (NSFC) under grants 41504123, and the 111 Project (grant No. B17035). The data used in this study were obtained from the MMS Science Data Center (https://lasp.colorado.edu/mms/sdc/public/). We thank the MMS teams for the high-quality data and successful operation. The French involvement (SCM) on MMS is supported by CNES and CNRS.

References

Anderson, L., Erlandson, R. E., & Zanetti, L. J. 1992, JGR, 97, 3089
Andersson, L., Ergun, R. E., Tao, J., et al. 2009, PhRvL, 102, 225004
Baker, D. N., Higbie, P. R., Hones, E. W., Jr., & Belian, R. D. 1978, JGR, 83, 4863
Birn, J., & Hesse, M. 2005, AnGeo, 23, 3365
Breuillard, H., Le Conte, O., REtino, A., et al. 2016, GeoRL, 43, 7279
Burch, J. L., Moore, T. E., Torbert, R. B., & Giles, B. L. 2016, SSRv, 199, 5
Chen, Z. Z., Fu, H. S., Liu, C. M., et al. 2019, GeoRL, 46, 5698
Davidson, R. C., Gladd, N. T., Wu, C. S., & Huba, J. D. 1977, PhFl, 20, 301
Deng, X., Ashour-Abdalla, M., Zhou, M., et al. 2010, JGRA, 115, 09225
Divin, A., Khotyaintsev, Y. V., Vaivads, A., & André, M. 2015, JGRA, 120, 1124
Dunlop, M., Balogh, A., Glassmeier, K. H., & Robert, P. 2002, JGR, 107, 1384
Ergun, R. E., Tucker, S., Westfall, J., et al. 2016, SSRv, 199, 167
Fu, H. S., Cao, J. B., Cully, C. M., et al. 2014, JGRA, 119, 9089
Fu, H. S., Cao, J. B., Khotyaintsev, Y. V., et al. 2013b, GeoRL, 40, 6023
Fu, H. S., Chen, F., Chen, Z. Z., et al. 2020, PhRvL, 124, 095101
Fu, H. S., Khotyaintsev, Y. V., André, M., & Vaivads, A. 2011, GeoRL, 38, L16104
Fu, H. S., Khotyaintsev, Y. V., Vaivads, A., et al. 2012c, JGR, 117, A12221
Fu, H. S., Khotyaintsev, Y. V., Vaivads, A., et al. 2013a, NatPh, 9, 426
Fu, H. S., Khotyaintsev, Y. V., Vaivads, A., André, M., & Huang, S. Y. 2012a, GeoRL, 39, L06105
Fu, H. S., Khotyaintsev, Y. V., Vaivads, A., André, M., & Huang, S. Y. 2012b, GeoRL, 39, L10101
Fu, H. S., Xu, Y., Vaivads, A., & Khotyaintsev, Y. V. 2019, ApJL, 870, L22
Gary, S. P., Gerwin, R. A., & Forslund, D. W. 1976, PhFl, 19, 579
Harvey, C. C. 1998, in Analysis Methods for Multi-Spacecraft Data, ed. G. Paschmann & P. Daly (Noordwijk: ESA), 307
Huang, S. Y., Yuan, Z. G., Ni, B., et al. 2015, JASTP, 129, 119
Huang, S. Y., Zhou, M., Deng, X. H., et al. 2012, AnGeo, 30, 97
Huba, J. D., Gladd, N. T., & Papadopoulos, K. 1978, JGR, 83, 5217
Khotyaintsev, Y. V., Cully, C. M., Vaivads, A., André, M., & Owen, C. 2011, PhRvL, 106, 165001
Le Contel, O., Nakamura, R., Breuillard, H., et al. 2017, JGRA, 112, 12236
Le Contel, O., Leroy, P., Roux, A., et al. 2016, SSRv, 199, 257
Li, H., Zhou, M., Deng, X., et al. 2015, JGRA, 120, 1086
Liang, J., Jiang, F., Donovan, E., et al. 2013, AnGeo, 31, 1077
Lindqvist, P. A., Olsson, G., Torbert, R. B., et al. 2016, SSRv, 199, 137
Liu, C. M., Fu, H. S., Cao, D., et al. 2018a, ApJ, 860, 128
Liu, C. M., Fu, H. S., Xu, Y., et al. 2017, JGRA, 122, 594
Liu, C. M., Fu, H. S., Xu, Y., et al. 2018b, GeoRL, 45, 556
Liu, C. M., Fu, H. S., Xu, Y., et al. 2018c, GeoRL, 45, 4628
Lu, Q. M., Lembege, B., Tao, J. B., & Wang, S. 2008, JGR, 113, A11219
Man, H. Y., Zhou, M., Deng, X. H., et al. 2018, GeoRL, 45, 8729
Mozer, F. S., Agapitov, O. V., Artemyev, A., et al. 2015, GeoRL, 42, 3627
Nakamura, R., Baumjohann, W., Klecker, B., et al. 2002, GeoRL, 29, 1942
Nishimura, Y., Bortnik, J., Li, W., et al. 2010, Sci, 330, 81
Norgren, C., Vaivads, A., Khotyaintsev, Y. V., & André, M. 2012, PhRvL, 109, 055001
Ohtani, S. 2004, SSRv, 113, 77
Panov, E. V., Artemyev, A. V., Baumjohann, W., Nakamura, R., & Angelopoulos, V. 2013, JGRA, 118, 3065
Perraut, S., Le Contel, O., Roux, A., & Pedersen, A. 2000, JGR, 105, 21097
Pollock, C., Moore, T., Jacques, A., et al. 2016, SSRv, 199, 331
Pritchett, P. L., Coroniti, F. V., & Nishimura, Y. 2014, JGRA, 119, 4723
Rönnmark, K. 1982, WHAMP-Waves in Homogeneous, Anisotropic, Multicomponent Plasmas Kiruna Geophysical Institute Rep. 179, (Kiruna: Kiruna Geophysical Institute)
Runov, A., Angelopoulos, V., Sitnov, M. I., et al. 2009, GeoRL, 36, L14106
Russell, C. T., Anderson, B. J., Baumjohann, W., et al. 2016, SSRv, 199, 189
Santolík, O., Parrot, M., & Lefeuvre, F. 2003, RaSc, 38, 1010
Schmid, D., Volwerk, M., Nakamura, R., Baumjohann, W., & Heyn, M. 2011, AnGeo, 29, 1537
Torbert, R. B., Russell, T. C., Magnes, W., et al. 2016, SSRv, 199, 105
Umeda, T., Omura, Y., Miyake, T., Matsumoto, H., & Ashour-Abdalla, M. 2006, JGR, 111, A10206
Vasko, I. Y., Agapitov, O. V., Mozer, F., Artemyev, A. V., & Jovanovic, D. 2015, GeoRL, 42, 2123
Wang, J., Cao, J. B., Fu, H. S., Liu, W. L., & Lu, S. 2017, JGRA, 122, 185
Xu, Y., Fu, H. S., Liu, C. M., & Wang, T. Y. 2018, ApJ, 853, 11
Xu, Y., Fu, H. S., Norgren, C., et al. 2019, GeoRL, 46, 7883
Yang, J., Cao, J. B., Fu, H. S., et al. 2017, JGRA, 122, 4299
Yao, Z., Fazakerley, A. N., Varsani, A., et al. 2016, JGRA, 121, 5185

Yu, X., Yuan, Z., Wang, D., et al. 2015, GeoRL, 42, 1312
Yu, X., Yuan, Z., Wang, D., et al. 2016, JGRA, 121, 11101
Yuan, Z., Yu, X., Wang, D., et al. 2016, JGRA, 121, 6711
Zhang, X., Angelopoulos, V., Pritchett, P. L., & Liu, J. 2017, JGRA, 122, 5247
Zhang, X. J., & Angelopoulos, V. 2014, JGRA, 119, 2536
Zhao, M. J., Fu, H. S., Liu, C. M., et al. 2019, GeoRL, 46, 2390
Zhong, Z. H., Deng, X. H., Zhou, M., et al. 2019, GeoRL, 46, 12693
Zhou, M., Ashour-Abdalla, M., Deng, X., et al. 2009a, GeoRL, 36, L20107
Zhou, M., Ashour-Abdalla, M., Deng, X., et al. 2017, JGRA, 122, 9513
Zhou, M., Berchem, J., Walker, R. J., et al. 2018, JGRA, 123, 1834
Zhou, M., Deng, X., Ashour-Abdalla, M., et al. 2013, JGRA, 118, 674
Zhou, M., Deng, X. H., Li, S. Y., et al. 2009b, JGRA, 114, A02216
Zhou, M., Huang, J., Man, H. Y., et al. 2019, ApJL, 872, L26
Zhou, M., Ni, B., Huang, S., et al. 2014, JGRA, 119, 4335
Zhou, M., Pang, Y., Deng, X. H., Yuan, Z. G., & Huang, S. Y. 2011, JGRA, 116, A06222